Journal of Physics D: Applied Physics

Influence of $Al_xGa_{1-x}N$ nucleation layers on MOVPE-grown zincblende GaN epilayers on 3C-SiC/Si(001)

To cite this article before publication: Abhiram Gundimeda *et al* 2022 *J. Phys. D: Appl. Phys.* in press https://doi.org/10.1088/1361-6463/ac4c58

Influence of $Al_xGa_{1-x}N$ nucleation layers on MOVPE-grown zincblende GaN epilayers on 3C-SiC/Si(001)

Abhiram Gundimeda[1,*], Mohammadreza Rostami[1, 2], Martin Frentrup[1], Alexander Hinz[1], Menno J. Kappers[1], David J. Wallis[1, 3], Rachel A. Oliver[1]

[1] Department of Materials Science and Metallurgy, University of Cambridge, 27 Charles Babbage Rd, Cambridge, CB3 0FS, United Kingdom
[2] Department of Materials Science and Engineering, EPFL – MXF 112, Station 12, CH–1015, Lausanne, Switzerland
[3] Centre for High Frequency Engineering, University of Cardiff, 5 The Parade, Newport Road, Cardiff, CF24 3AA, United Kingdom
Corresponding author: ag2025@cam.ac.uk

Abstract

The suitability of $Al_xGa_{1-x}N$ nucleation layers with varying Al fraction x for the metal organic vapour phase epitaxy of zincblende GaN on (001) 3C-SiC was investigated, using X-ray photoelectron spectroscopy, atomic force microscopy, and X-ray diffraction. The as-grown nucleation layers exhibited elongated island structures on their surface, which reduce laterally into smaller, more equiaxed islands with increasing AlN composition. During high-temperature annealing in a mixture of NH_3 and H_2 the nucleation islands with low Al fraction ripened and increased in size, whereas this effect was less pronounced in samples with higher Al fraction. The compressive biaxial in-plane strain of the nucleation layers increases with increasing AlN composition up to x = 0.29. GaN epilayers grown over nucleation layers that have low Al fraction have high cubic zincblende phase purity and are slightly compressively strained relative to 3C-SiC. However, those samples with a measured Al fraction in the nucleation layer higher than 0.29 were predominantly of the hexagonal wurtzite phase, due to formation of wurtzite inclusions on various {111} facets of zb-GaN, thus indicating the optimal Al composition for phase-pure zb-GaN epilayer growth.

Keywords: AlGaN, Nucleation layers, zincblende, surface morphology, phase purity

1. Introduction

Hexagonal, wurtzite (wz)-phase III-Nitride material systems have been extensively used for various optoelectronic applications, and their widespread usage in lighting has delivered significant worldwide electricity savings. However, at present, the efficiency of green-wavelength LEDs is only about half of that of InGaAsP-based red- and nitride-based blue-wavelength LEDs, which is also known as the 'green gap' problem [1]. This is partially related to the presence of piezoelectric and spontaneous polarisation fields in wurtzite nitride heterostructures, resulting in the quantum confined Stark effect when grown in the (0001) orientation. These fields increase with increasing In-content (which is required to achieve green emission) and reduce the overlap of the electron and hole wavefunctions in the active region, which impairs the device efficiencies. Cubic, zincblende (zb)-phase $In_xGa_{1-x}N$/GaN heterostructures have the potential to bridge the 'green gap' due to the predicted absence of spontaneous and piezoelectric polarisation fields in the (001) orientation [2]. Beyond potential optoelectronic usage the effective electron mass for zb-GaN ($0.13m_o$) is smaller than that for wz-GaN ($0.20m_o$), which makes it a potential candidate for efficient high speed power electronic devices, like ultrafast field effect transistors [3, 4]. However, growth [5], optical [6, 7] and electrical properties [8] of zb-GaN thin films can be affected by the presence of wurtzite inclusions, high densities of planar {111} stacking faults, and misfit dislocations [5]. Extensive research has been carried out on the growth of zb-GaN on GaAs (001) [9-15], 3C-SiC (001) [16-23] and 3C-SiC/Si (001) [24-30]. In particular, recent developments of high-quality, large area 3C-SiC/Si (001) heteroepitaxial templates may present an alternative route for zb-GaN growth by metalorganic vapour phase epitaxy (MOVPE).

To date, growth of zb-GaN on 3C-SiC/Si (001) has resulted in films with high density of stacking faults which often arise from dissociated misfit dislocations, formed at the heterointerface between zb-GaN and 3C-SiC to compensate the lattice mismatch of 3.4 % between both materials [29]. Introducing a zb-AlN nucleation layer (NL) (lattice mismatch of 0.3 %) or zb-$Al_xGa_{1-x}N$ NL with an intermediate lattice constant between 3C-SiC and zb-GaN, may help to reduce the lattice mismatch with 3C-SiC, thereby potentially reducing the stacking fault density in the zb-GaN layer [31]. In addition to the lattice mismatch issue, the difference between the thermal expansion coefficients of Si, 3C-SiC and zb-GaN lead to additional thermal strain in the film after cooling down from growth temperature, which may lead to cracking of the thin film. The same crucial problem encountered for the growth of conventional wz-GaN on (111) Si has been overcome using AlN NLs and graded $Al_xGa_{1-x}N$ buffer layers for strain management prior to the GaN layer growth [32]. This might therefore be the route of choice for the development of crack-free, large area zb-GaN thin films.

However, the available literature shows that obtaining high phase purity zb-$Al_xGa_{1-x}N$ is a challenge: The growth of zb-$Al_xGa_{1-x}N$ epilayers on 3C-SiC (001) substrates with zb-AlN NL layers over the whole $Al_xGa_{1-x}N$ compositional range was attempted by MBE [33, 34]. Even though the lattice constants of the cubic $Al_xGa_{1-x}N$ alloys measured via x-ray diffraction

(XRD) obey Vegard's law, no significant data on either surface morphology or phase purity were presented. The difficulties in achieving zb phase purity for the AlN growth on 3C-SiC (001) at low- or high temperature [35] were ascribed to the relative stability of the zb and wz phases of AlN and GaN as outlined by Städele *et al.* [36] who calculated a total energy difference between the zb and wz phases in AlN of 28.9 meV/atom compared to 10.2 meV/atom in GaN. Although the growth of AlN may be energetically less favourable than GaN on 3C-SiC, As *et al.* [37, 38] successfully grew high-quality zb-$Al_xGa_{1-x}N$ films by MBE after a careful cleaning routine of the substrate surface. Encouraged by these recent results, we investigate here the use of zb-$Al_xGa_{1-x}N$ nucleation layers for zb-GaN growth on 3C-SiC (001) by MOVPE, focussing on the phase purity and surface morphology of the resulting epitaxial layers.

2. Experimental details:

In this study, the $Al_xGa_{1-x}N$ NLs and GaN epilayers were grown by metalorganic vapour-phase epitaxy (MOVPE) on 3C-SiC/Si (001) substrates in a 6 × 2" Thomas Swan close-coupled showerhead reactor. The substrates, provided by Anvil Semiconductors Ltd., consisted of a 3.5 µm thick layer of 3C-SiC grown on a 750 µm thick Si wafer with 4° miscut towards the [110] in-plane direction to prevent the formation of antiphase domains [30]. The precursors for growth are trimethylgallium (TMG), trimethylaluminium (TMAl), ammonia (NH_3) as Ga, Al, and N sources, respectively, while hydrogen was used as the carrier gas. The in-situ monitoring of the growth temperatures was performed using emissivity-corrected optical pyrometry and the growth rates were measured using in-situ three wavelength reflectance transients with the relevant optical constants provided by LayTec AG.

Prior to the growth of the nucleation layers, the growth rate of GaN (AlN) was measured as 0.27 nm/s using a TMG flow of 89 µmol/min (TMA flow of 173 µmol/min) under standard NL growth conditions and a temperature of 600°C. The relatively high TMA flow suggests that parasitic gas phase reactions were severe under those conditions. To vary the composition of the $Al_xGa_{1-x}N$ NLs, the precursor flow rates were changed linearly between these two binary reference conditions thereby assuming a constant growth rate across the compositional range. The thickness was targeted to be around 22 nm, which was previously found to be an optimal thickness for zb-GaN NLs [39]. However, when the layer thicknesses of the $Al_xGa_{1-x}N$ NLs studied here were measured by transmission electron microscopy, they were found to be around 15 nm. The reduced thickness can be explained by additional parasitic pre-reaction between the Al- and Ga precursors, which reduces the total incorporation efficiency and hence reduced the alloy growth rate [40, 41].

Three sets of samples were grown, for which the nominal composition of the $Al_xGa_{1-x}N$ NL was varied, as shown in Fig. 1. In the first sample series, the thin $Al_xGa_{1-x}N$ NLs were grown directly on the 3C-SiC/Si substrate with a nominal Al fraction x of 0, 0.25, 0.50, 0.75, and 1, and cooled down immediately to room temperature after growth. The second

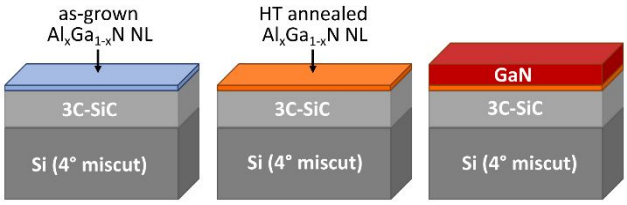

Figure 1: Schematic of different set of samples grown on 4° miscut 3C-SiC/Si substrates (a) as-grown $Al_xGa_{1-x}N$ nucleation layers, (b) annealed $Al_xGa_{1-x}N$ nucleation layers and (c) zb-GaN epilayer grown on annealed $Al_xGa_{1-x}N$ nucleation layers.

sample series underwent an additional high temperature treatment in an atmosphere of NH_3 and H_2 to mimic the temperature ramp to 880°C used for zb-GaN buffer growth (Fig. 1 (b)) and were then cooled down to room temperature. To investigate the effect of the Al fraction in the NL on overgrown GaN epilayers, a third set of samples was grown. This series consists of $Al_xGa_{1-x}N$ NLs which were annealed under the same conditions as sample series 2 and then overgrown with 600 nm thick GaN epilayers at 880°C as shown in Fig. 1 (c). For this third sample series, a broader range of $Al_xGa_{1-x}N$ NL compositions has been considered (nominal x = 0, 0.12, 0.25, 0.37, 0.5, 0.62, 0.75, 1).

To determine the Al fraction in the NLs, X-ray photoemission spectroscopy (XPS) measurements were performed with an Escalab 250Xi spectrometer using a monochromatic Al-K_α (1486.7 eV) radiation source. To remove carbon and oxygen surface contamination the samples underwent an in-situ sputtering prior to the XPS measurements. Charging effects were accounted for by using the C 1s peak as a reference.

The surface morphologies of the $Al_xGa_{1-x}N$ NLs and GaN thin films were investigated by atomic force microscopy (AFM) with a Bruker Dimension Icon Pro in PeakForce tapping mode using Bruker SCANASYST-AIR tips. The fast scan direction was aligned along the [110] miscut direction for all samples. The free-software WSxM [42] was then utilized to analyse the topographic data and calculate the RMS roughness. A 2D fast Fourier transform (FFT) approach was used to determine the in-plane dimensions of the surface features as described in Reference [30]. The RMS roughness and in plane feature size for each sample were calculated across five different areas on the surface and the average of these five values is presented. For the uncertainty of the RMS value, the standard error of the mean from these five measurements was used.

X-ray diffraction (XRD) was used to investigate the crystallographic properties of the samples. A Philips X'pert diffractometer equipped with a 4-crystal Bartels monochromator (λ = 1.54056 Å), an adjustable crossed slits collimator, and a gas-proportional detector was employed to perform ω-2θ-scans of the 002 zb-$Al_xGa_{1-x}N$ reflection for the NLs. Pseudo-Voigt fits of these scans were performed to determine the 2θ Bragg-angle of the $Al_xGa_{1-x}N$ peaks, which were then used to obtain the out-of-plane lattice parameter c of the (partially strained) NLs and to calculate the bi-axial in-plane strain of the $Al_xGa_{1-x}N$ NL (ε_x). As a reference, the

theoretical lattice parameters of relaxed material as well as its elastic constants have been calculated using alloy compositions from the XPS analysis and assuming a linear dependence between the parameters of zb-GaN (a = 4.50597(38) Å, C_{11} = 293 GPa, C_{12} = 159 GPa) and zb-AlN (a = 4.3714 Å, C_{11} = 304 GPa, C_{12} = 160 GPa) [29]. From these values the in-plane strain of the $Al_xGa_{1-x}N$ NL ε_x was calculated by the relation $\varepsilon_z = -2 \times (C_{12}/C_{11}) \times \varepsilon_x$ assuming the strain is biaxial [29]. Although the growth was performed on 3C-SiC/Si templates with a miscut which might lead to a slightly anisotropic in-plane strain, this is a reasonable assumption given that such an anisotropy has been observed to be only very small in thicker zb-GaN samples [29] and alternative approaches to measure the in-plane strain directly from off-axis reflections were too imprecise for the investigated NLs.

To compare the mosaicity of the GaN thin films grown on the $Al_xGa_{1-x}N$ NLs, the full width at half maximum of ω-scans (ω-FWHM) of the 002 reflection was measured with the beam path plane parallel and perpendicular to the miscut direction, respectively. On these samples, texture maps of the $1\bar{1}03$ wz reflections were performed to investigate the preferred orientation of any hexagonal inclusions present in the samples with respect to the sample miscut. For a more detailed phase quantification a PANalytical Empyrean diffractometer with two-bounce hybrid monochromator, 1/4° primary beam slit, and PIXcel solid-state area detector was employed to measure large area reciprocal space maps of the 113 zb-GaN and $1\bar{1}03$ wz-GaN reflections, following the approach described elsewhere [29].

3. Results and Discussion

3.1. As-grown and annealed $Al_xGa_{1-x}N$ NLs

The compositions of the annealed nucleation layers were estimated using XPS. From XPS core level spectra, the Ga (3d) peaks were deconvoluted into the Ga-N and Ga-O components, and the Al (2p) peaks were deconvoluted into their Al-N and Al-O components using Voigt-functions [43], as shown in Figure 2 (a) and (b) for the NL with a nominal Al fraction x = 0.75. The integrated intensities of the fitted Ga 2s and Al 2p peaks were then used to calculate the Al fractions of the alloys, as presented in Fig. 2 (c). To exclude effects from the preferential oxidation of Al compared to Ga the sum of both nitride and oxide peaks were used in the determination of the Al fraction. This is justified as it is unlikely that large amounts of metallic Al or Ga were present in the nucleation layers prior to exposure to the ambient atmosphere. Thus, all the oxidised metallic species were part of the nitride layers. Given that in the case of the samples with a nominal Al fraction of x = 0.25 we do not observe a notable difference between the Al fractions as obtained by XPS for the as-grown (≈ 0.01) and annealed NLs (≈ 0.02). One can conclude that there is also no substantial enrichment of Al at the surface due to preferential desorption of Ga during the annealing at 880 °C. Figure 2 (c) provides a comparison between the nominal Al fraction based on the growth conditions and the Al fraction incorporated into the annealed NLs as measured from XPS. It is quite evident that the measured Al fractions strongly deviate from the nominal Al fraction highlighted by the dashed line, revealing that the Al incorporation was particularly inefficient under relatively Ga-rich conditions.

For the annealed $Al_xGa_{1-x}N$ NL with nominal Al fraction x = 0.25, the actual Al fraction determined by XPS was only x = 0.02. Above this nominal Al fraction of x = 0.25, the actual Al fraction of the NLs shows an approximately linear increase with higher nominal Al fraction up to 0.95 for the nominally pure AlN NL. As pointed out above there is no significant deviation between measured fractions of as-grown and annealed NLs so that their deviation from the nominal values cannot be related to the annealing procedure. Instead, the observed low Al-incorporation efficiency is likely related to parasitic gas phase reactions of the group-III precursors in the reactor [40, 41]. Other effects, like memory effects from the reactor walls, may contribute to the contamination of the nominally pure AlN NL with GaN. For the third set of samples, a larger range of $Al_xGa_{1-x}N$ compositions in the NLs was used, compared to the previous as-grown and annealed NL series. As the $Al_xGa_{1-x}N$ NLs are buried beneath GaN epilayers in the third sample series, it is not possible to use XPS to estimate the Al fraction of these NLs. Hence NL compositions were assumed to be the same as the annealed NL series and a polynomial fit was used on the measured XPS

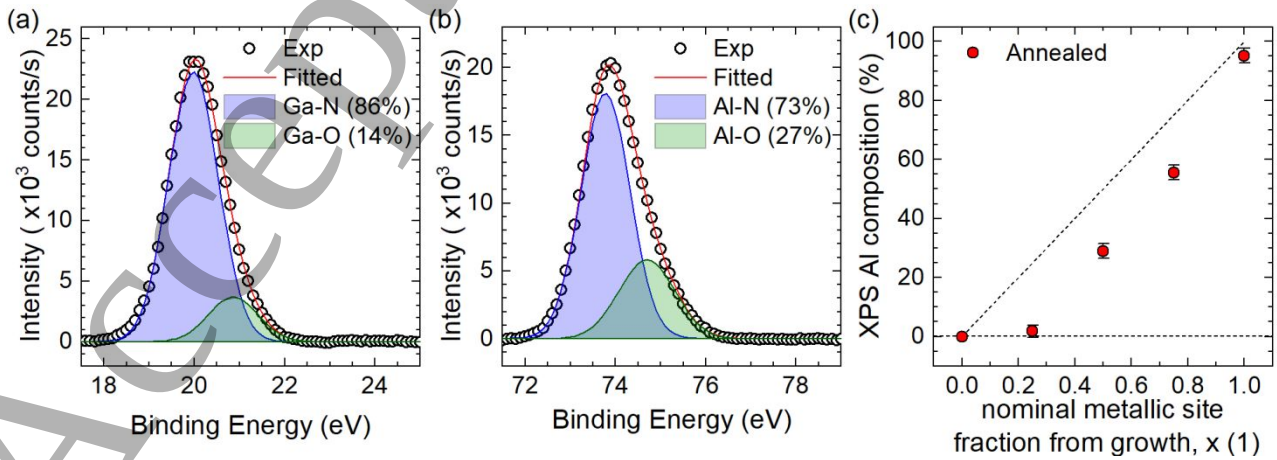

Figure 2: XPS core level spectra of (a) Ga 3d and (b) Al 2p for an $Al_xGa_{1-x}N$ NL with a nominal Al fraction x = 0.75. (c) 1:1 ratio plot illustrating the comparison of the Al fraction obtained from XPS and the nominal fraction determined from input flow rates.

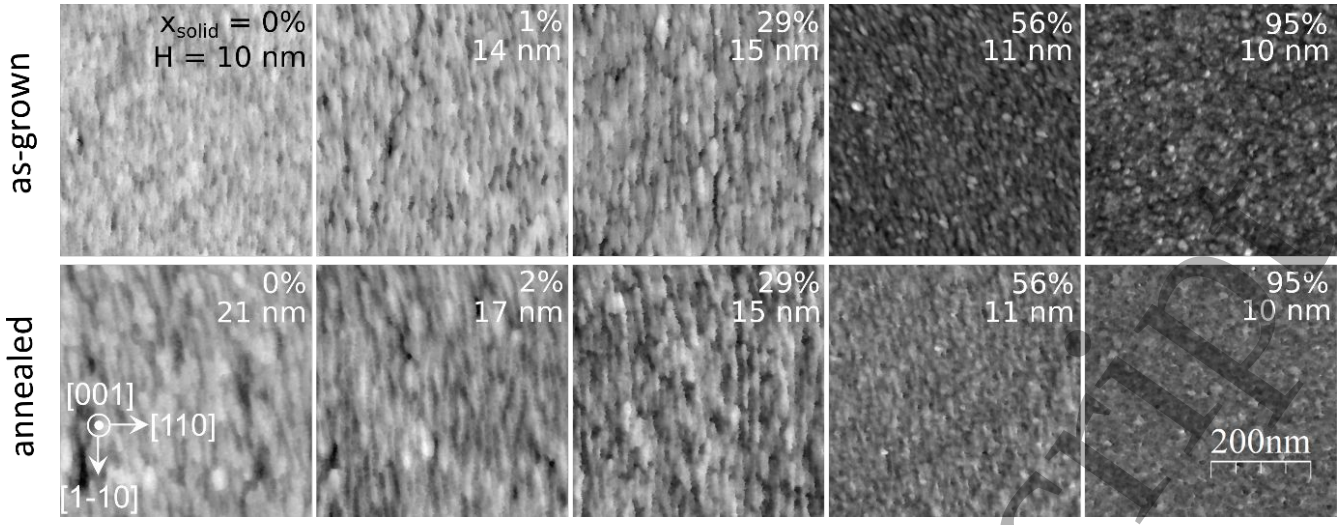

Figure 3: AFM images (500 × 500 nm^2) of as-grown (top row) and annealed (bottom row) $Al_xGa_{1-x}N$ NLs with varying Al composition grown on 3C-SiC/Si substrates. The XPS compositions and feature heights (H) are shown in each image.

values to calculate expected Al fractions of ~0.01, ~0.13, and ~0.40 for the additional NLs with 0.12, 0.37, and 0.62 nominal Al fractions, respectively. The GaN epilayers grown on these NLs will be discussed in more detail later in section 3.2.

The AFM images in Figure 3 show the change in surface morphology of the as-grown and annealed $Al_xGa_{1-x}N$ NLs with Al fraction. The XPS-measured composition of each sample, as well as the height range (H) in the image corresponding to the full colour scale from black to white, are indicated in each image. The as-grown NLs (top row) exhibit elongated surface features along $[1\bar{1}0]$ for an Al fraction up to 0.29. Previous studies suggest that such elongated features may be formed by anisotropic diffusion related to the reduced crystal symmetry on the (001) surface [30]. At higher Al fractions of 0.56 and 0.95, the surface transformed from elongated striations along $[1\bar{1}0]$ to rounded granular structures. This change in morphology with increasing Al fraction could be indicative of more isotropic diffusion in zb-$Al_xGa_{1-x}N$ than zb-GaN, and to lower diffusion lengths across the board in cubic $Al_xGa_{1-x}N$. The RMS roughness of the as-grown nucleation layers estimated by averaging the roughness for five different regions across each sample is shown in Fig. 4 (a). The root mean square (RMS) roughness, which is (0.85 ± 0.01) nm for the as-grown GaN NL increases with increasing Al fraction and peaks at (2.00 ± 0.08) nm at an Al fraction of x = 0.29. Then the RMS roughness reduced gradually to (0.90 ± 0.03) nm for the nearly pure AlN NL.

The effect of high temperature treatment in H_2 and NH_3 on the surface morphology of the $Al_xGa_{1-x}N$ NLs is shown in the bottom row of Fig. 3. Similar to the as-grown nucleation layers, the surface transformed from elongated features along $[1\bar{1}0]$ to rounded granular structures with increasing Al fraction. For NLs with Al fraction greater than 0.02, the RMS roughness of the annealed NLs was lower than for the as-grown NLs of similar composition, indicating a slight smoothing of the surfaces after annealing. At lower Al fractions the RMS roughness increased on annealing, indicating significant surface roughening. To further compare the effect of high temperature annealing on the surface morphology between the NL sample series and across the compositional range, 2D-FFT analyses have been employed to determine the typical widths of the surface feature along the [110] direction. Initially, for as-grown NLs, the change in feature size is minimal with the average size of the features calculated to be around 40 nm (Fig. 4 (b)). The size of the surface features on the annealed NLs is larger than that of the as-grown samples, but the difference decreases with higher Al

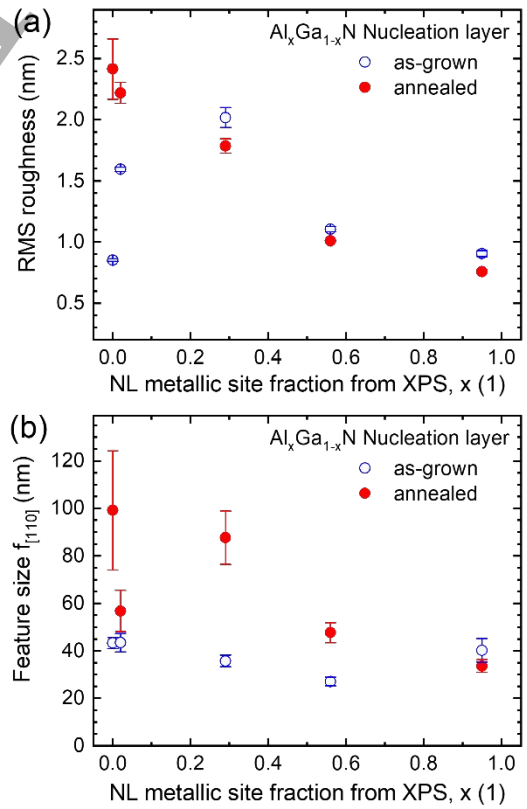

Figure 4: (a) variation in RMS roughness of the as-grown and annealed $Al_xGa_{1-x}N$ nucleation layers with varying Al fraction from XPS. and (b) variation in feature size along [110] direction of the as-grown and annealed $Al_xGa_{1-x}N$ NLs with varying Al fraction obtained from XPS

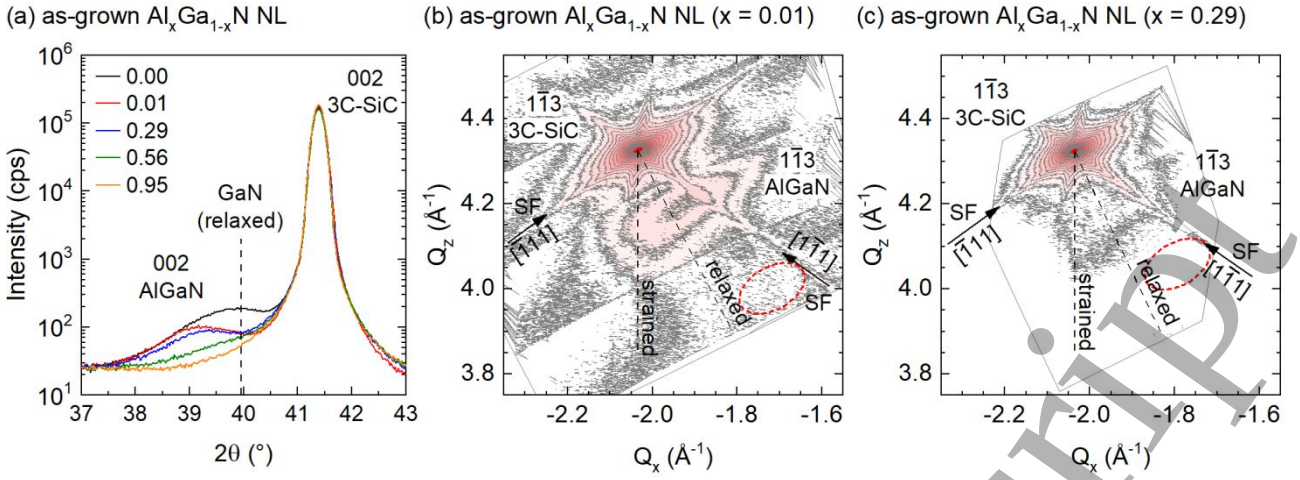

Figure 5: (a) XRD 2θ-ω scans showing zb-$Al_xGa_{1-x}N$ (002) and 3C-SiC (002) reflections of as-grown $Al_xGa_{1-x}N$ nucleation layers. The dashed line signifies the position of relaxed zb-GaN. (b-c) 2D Reciprocal space maps around the $1\bar{1}3$ zb-$Al_xGa_{1-x}N$ reflection in perpendicular to miscut direction along with $[\bar{1}11]_{zb}$ and $[1\bar{1}1]_{zb}$ stacking fault streaks for as-grown $Al_xGa_{1-x}N$ nucleation layer with Al fraction of (b) 0.01 and (c) 0.29 (Red circle indicates the expected position of the wz- $Al_xGa_{1-x}N$ reflection).

fraction. This could be related to the ripening of islands, i.e., the diffusion of material from smaller islands to larger islands. As Ga adatoms have a lower sticking coefficient than Al adatoms, this effect is expected to be more significant for GaN-rich/AlN-poor NLs, where the atoms are more mobile leading to the formation of larger islands [44]. It is noted that in all samples the entire SiC surface is covered by the $Al_xGa_{1-x}N$ NL despite a suboptimal thickness of ca. 15nm. In previous work [45] it was observed that an incomplete coverage by the NL resulted in the formation of wz inclusions within the zb-GaN epilayer.

XRD 2θ-ω measurements were performed to analyze the structural properties of the $Al_xGa_{1-x}N$ NLs. Fig 5 (a) shows the 2θ-ω scans collected in the range between 37° and 43° of the as-grown $Al_xGa_{1-x}N$ NLs. The intense peak at 41.39° corresponds to the 002 reflection of the 3C-SiC template, and the weak 002 reflections on the low angle side indicate that the $Al_xGa_{1-x}N$ NLs (apart from the AlN NL) have the zb-phase. With increasing Al fraction, the intensity of the $Al_xGa_{1-x}N$ peaks become weaker due to the lower scattering efficiency of Al compared to Ga. However, as the integrated intensity of the X-ray reflections is proportional to the material volume [29], the low intensity of the $Al_xGa_{1-x}N$ reflections for the samples with a high Al fraction might also reflect a decline in phase purity.

As the wurtzite phase gives no reflections in XRD 2θ-ω scans at these angles, reciprocal space maps around the $1\bar{1}3$ zb-GaN and $1\bar{1}03$ wz-GaN reflections have been measured instead. Figure 5 (b) and 5 (c) show such reciprocal space maps for two of the as-grown $Al_xGa_{1-x}N$ nucleation layer samples with Al fractions of x = 0.01 and x = 0.29, respectively. Apart from the highly intense 3C-SiC $1\bar{1}3$ reflection, low-intensity streaks running along $[\bar{1}11]_{zb}$ and $[1\bar{1}1]_{zb}$ are clearly visible. These occurred due to the diffuse scattering from $(\bar{1}11)_{zb}$ and $(1\bar{1}1)_{zb}$ stacking faults in the structure, where diffracted x-rays suffer an additional phase shift between the two sides of a stacking fault [29]. In both reciprocal space maps one can also observe a low-intensity reflection of the zb-phase of $Al_xGa_{1-x}N$, which becomes weaker and moves much closer to the 3C-SiC reflection as the AlN-content increases. However, both space maps show the absence of the $1\bar{1}03$ wz-$Al_xGa_{1-x}N$ reflection, whose theoretical position is indicated by the red circles. This shows that in these samples the wz phase is absent or only present in low concentrations. However, for the NL with Al fractions higher than 0.29 (not shown), the $1\bar{1}3$ $Al_xGa_{1-x}N$ reflections of the zb and wz phase are superimposed by the more intense 3C-SiC reflection and the SiC SF-streaks, so that they cannot be observed. As a result, definite information on the phase purity of the NL with higher Al fraction cannot be provided. TEM-based phase analysis investigations are currently underway and will be reported elsewhere.

To examine the strain state of the NLs, a detailed analysis into the 2θ-ω scans of the 002 reflection and the reciprocal space maps of the $1\bar{1}3$ zb-$Al_xGa_{1-x}N$ reflections for a sub-set of the samples was performed. The dotted line in Figure 5 (a) indicates the theoretical 2θ position of relaxed zb-GaN (2ϑ = 39.9845(35)°). Initially, the 2θ peak position of the GaN nucleation layer is at slightly lower Bragg angle than that of a

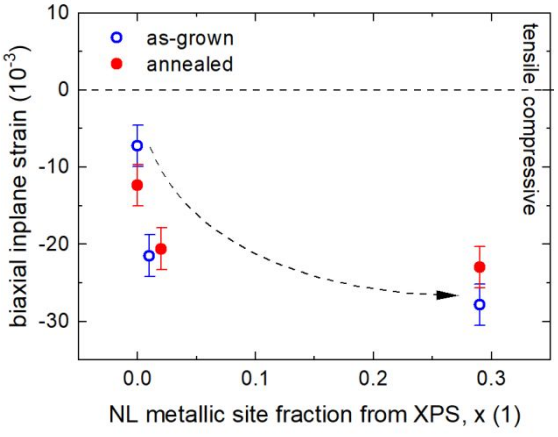

Fig 6: Change in bi-axial in-plane strain with increasing Al fraction of as-grown and annealed $Al_xGa_{1-x}N$ NLs.

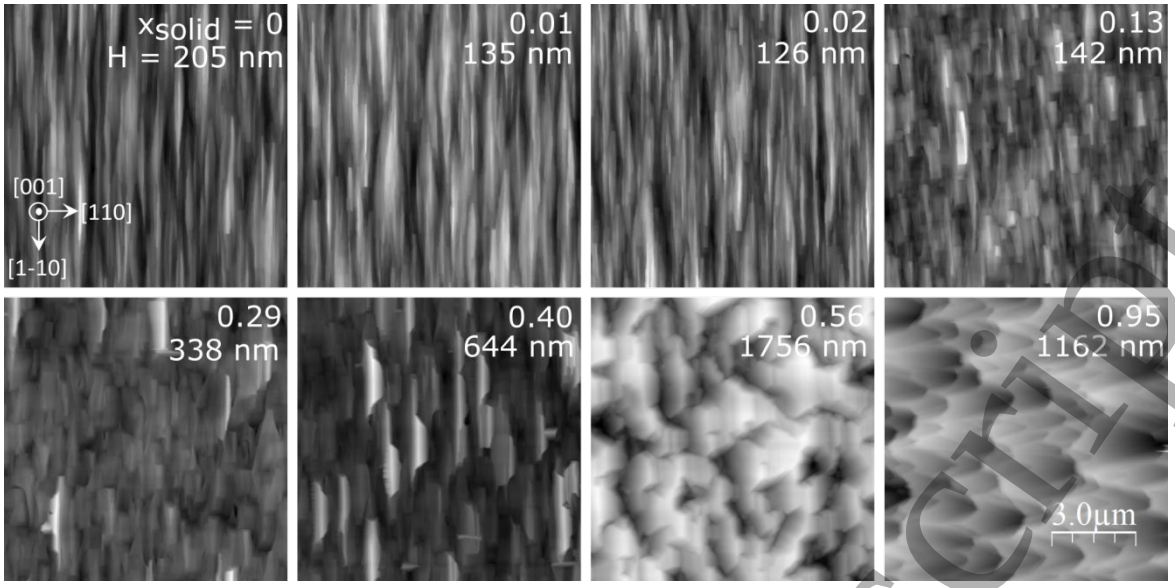

Figure 7: AFM images (10 × 10 µm²) of zb-GaN epilayer upon annealed $Al_xGa_{1-x}N$ nucleation layers grown on 3C-SiC/Si substrate with varying Al composition. The XPS compositions and feature heights (H) are shown in each image.

relaxed GaN layer indicating that it has a slightly higher lattice constant thereby revealing a minimal amount of compressive in-plane strain, on the order of 7×10^{-3} (Fig. 6). As the lattice constant of zb-$Al_xGa_{1-x}N$ is smaller than that of zb-GaN, with increasing Al fraction, the 002 x-ray reflections of the $Al_xGa_{1-x}N$ NLs in Figure 5 are expected to move towards the higher Bragg angle of the 3C-SiC peak linearly for relaxed layers. However, a non-linear shift in the peak positions with varying composition was observed. With increasing Al fraction, the 2θ-ω curves show a peak shift towards lower Bragg angles from the GaN peak for Al fractions of x = 0.01 and x = 0.29, indicating the presence of compressive in-plane strain in these samples with the highest strain of about 28×10^{-3} observed in the NL with x = 0.29 (Fig. 6). This is also confirmed by the position of the low-intensity broad $1\bar{1}3$ zb-$Al_xGa_{1-x}N$ reflection evident in the space map for the nucleation layer with an Al fraction of x = 0.01 in Fig. 5 (b), indicating that the nucleation layer has either a strain gradient from compressively strained to relaxed material or patches of material with different relaxation. Such behavior might seem surprising as zb-$Al_xGa_{1-x}N$ matches the 3C-SiC lattice much better than zb-GaN does. However, this comes with a larger critical thickness for $Al_xGa_{1-x}N$/SiC compared to GaN/SiC and may be the reason the thin nucleation layer does not fully relax. The change in in-plane strain between the annealed and as-grown nucleation layers is minimal (Fig. 6). Beyond Al fractions of x = 0.30 in the $Al_xGa_{1-x}N$ NL, the $Al_xGa_{1-x}N$ peaks in the 2θ-ω scans used for the strain analysis merge into the intense 3C-SiC substrate peak. Thus, no meaningful strain values could be determined for the NL samples with higher Al fractions than x = 0.30.

3.2. GaN epilayers on $Al_xGa_{1-x}N$ NLs

In the following section, we will investigate the influence of the annealed $Al_xGa_{1-x}N$ NLs with various Al fractions on the growth of 600 nm thick GaN epilayers on top of them. For this third series, 8 samples with Al fractions between 0 and 0.95 have been investigated. The variation in surface morphology of these GaN epilayers is shown in Fig. 7. As the Al fraction of the NLs increases, the surface of the GaN epilayers transformed from elongated striations along $[1\bar{1}0]$ to step like structures extended along [110] for the GaN epilayers with an AlN NL underneath. For the pure GaN NL and low Al

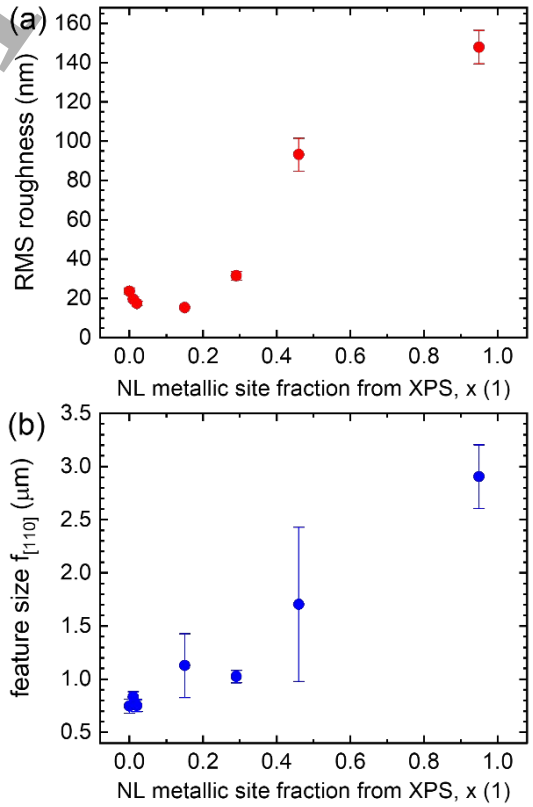

Figure 8: (a) Variation in RMS roughness in zb-GaN epilayers grown on $Al_xGa_{1-x}N$ nucleation layers with varying Al fraction and (b) Variation of surface feature size along [110] direction extracted from 2D-FFT of AFM height data of zb-GaN epilayers grown on $Al_xGa_{1-x}N$ nucleation layers with varying Al fraction.

fractions in the NL, the surface morphology of the GaN epilayer consists of striated islands along [1$\bar{1}$0]. The surfaces reveal shrinking of these striations along [1$\bar{1}$0] and extension along [110] with increasing Al fraction from x = 0 to x = 0.02. Compared to the NLs discussed in the previous section, these surface undulations are significantly larger and are around 0.8 µm in size along [110] up to x = 0.02, as shown in Fig. 8 (b). Surfaces with roughly rectangular blocks of about 1 µm width are formed for GaN grown on x = 0.13 and x = 0.29 $Al_xGa_{1-x}N$ NLs (Fig. 7). These were transformed into trapezoidal features on the surface at an Al fraction of x = 0.40. A complete change in surface morphology was observed for GaN epilayers with high Al fraction NLs, where large hexagonal shaped blocks of approx. 3 µm lateral size were observed (Fig. 7) for GaN on the x = 0.56 NL, and tilted pyramid-like structures forming a staircase along [110] when a NL with about x = 0.95 was used. Such drastic change in surface morphology in the epilayers at higher AlN-contents can be correlated with the change in surface morphologies in the nucleation layers, where the surface morphology revealed granular structures for Al fractions of x = 0.56 and x = 0.95. This change in surface morphology of the nucleation layers may have transformed the GaN epilayer surface morphology drastically.

The change in morphology from striations to surfaces with large rectangular or hexagonal shaped blocks, is also evident in the variation of the RMS surface roughness of 10 × 10 µm^2 AFM measurements of the GaN epilayer surface, shown in Fig. 8 (a). The RMS roughness initially decreases slightly from (23.6 ± 1.6) nm to (15.3 ± 0.2) nm with a small increase of the Al fraction, up to 0.13, of the NL. With further increase of the Al fraction the RMS roughness of the GaN epilayer increased steeply up to (147.9 ± 8.5) nm for GaN on a nucleation layer with an Al fraction of x = 0.95.

To quantify the crystalline quality of the zb-GaN epilayers, we have measured XRD ω-scans of the 002 zb-GaN reflection in directions both parallel and perpendicular to the sample miscut. Figure 9 (a) shows the ω-FWHM of the measured intensity peaks. No 002 reflection of the zb-GaN can be observed for the GaN epilayers grown with $Al_xGa_{1-x}N$ NLs above an Al fraction of x = 0.40 indicating that they are mostly of the wurtzite phase. Parallel to the miscut direction, the ω-FWHM value was 64 arcmin for the sample grown on the pure GaN NL. The peak broadening then fluctuated and reached the lowest value of 41.6 arcmin in case of the x = 0.13 NL, highlighting an improved quality. With further increase of the Al fraction in the $Al_xGa_{1-x}N$ NLs, a slight increase in the 002 ω-FWHMs of the GaN buffer to 69.1 arcmin and 72.3 arcmin for an Al fraction of x = 0.29 and x = 0.40, respectively can be observed, indicating a decline in crystalline quality. Perpendicular to the miscut direction, up to x = 0.13, the change in ω-FWHM of the GaN film on the $Al_xGa_{1-x}N$ NL is similar to that parallel to the miscut direction. Furthermore, perpendicular to the miscut direction, the ω-FWHM value was observed to be around 41 arcmin when a NL with x = 0.13 was used, which increased to 145 arcmin for x = 0.29 signifying poor crystalline quality in the zb-GaN film on top of the NL.

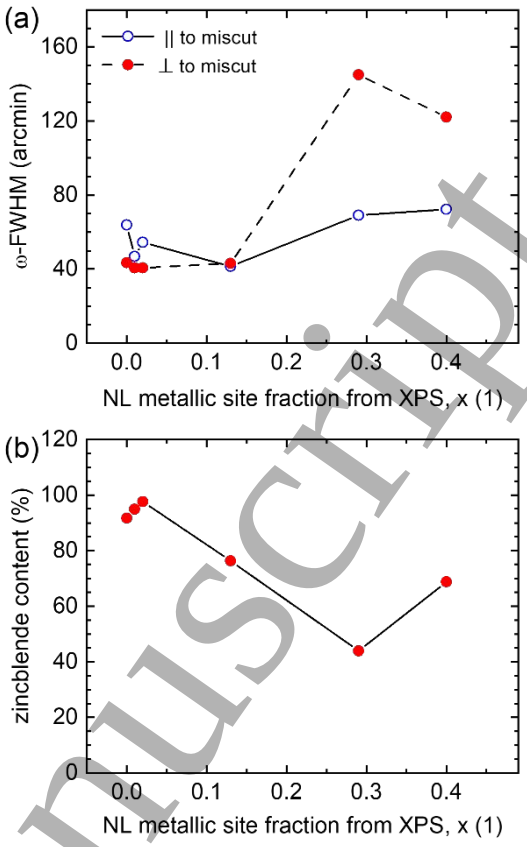

Figure 9: (a) Variation in 002 ω-FWHM of the zb-GaN epilayer measured parallel and perpendicular to the miscut direction as function of the Al fraction in the $Al_xGa_{1-x}N$ NL. (b) zb-GaN content in the epilayers determined by XRD as a function of the XPS measured Al fraction in the $Al_xGa_{1-x}N$ nucleation layers.

It is interesting to note that while the ω-FWHM values of the GaN epilayer for the two in-plane directions are very similar for low Al fractions in the NLs, their discrepancy strongly increases with increasing Al content. This suggest that the defect structure and the formation of possible wurtzite inclusions in the zb-GaN epilayers as main source for the reflection broadening (via diffuse streaking, see discussion in Ref. [29]) might be highly anisotropic.

In order to quantify the phase purity of zb-GaN films, we have measured 2D reciprocal space maps of the 1$\bar{1}$3 zb-GaN reflections both parallel and perpendicular to the miscut direction. The integrated intensities of the 113 zb-GaN and 1$\bar{1}$03 wz-GaN reflections were used to calculate the phase purity of the GaN epilayer, as shown in Fig. 9 (b). The zb-GaN phase purity was above 90% for the epilayer on $Al_xGa_{1-x}N$ NL with low Al fraction up to x = 0.02. Beyond this, the zb phase purity decreases and plunges to 44% and 69% at Al fractions of 0.29 and 0.40, respectively. For x = 0.56 and above in the NL, the grown GaN epilayer is completely wz.

In principle, such wurtzite inclusions and other defects related to stacking disorder can form on any of the four independent {111} planes in the zincblende crystal structure. However, previous studies with zb-GaN using GaN NLs indicate that this is not necessarily the case [30]. Instead, it has been found that the preferential site for such defects might be

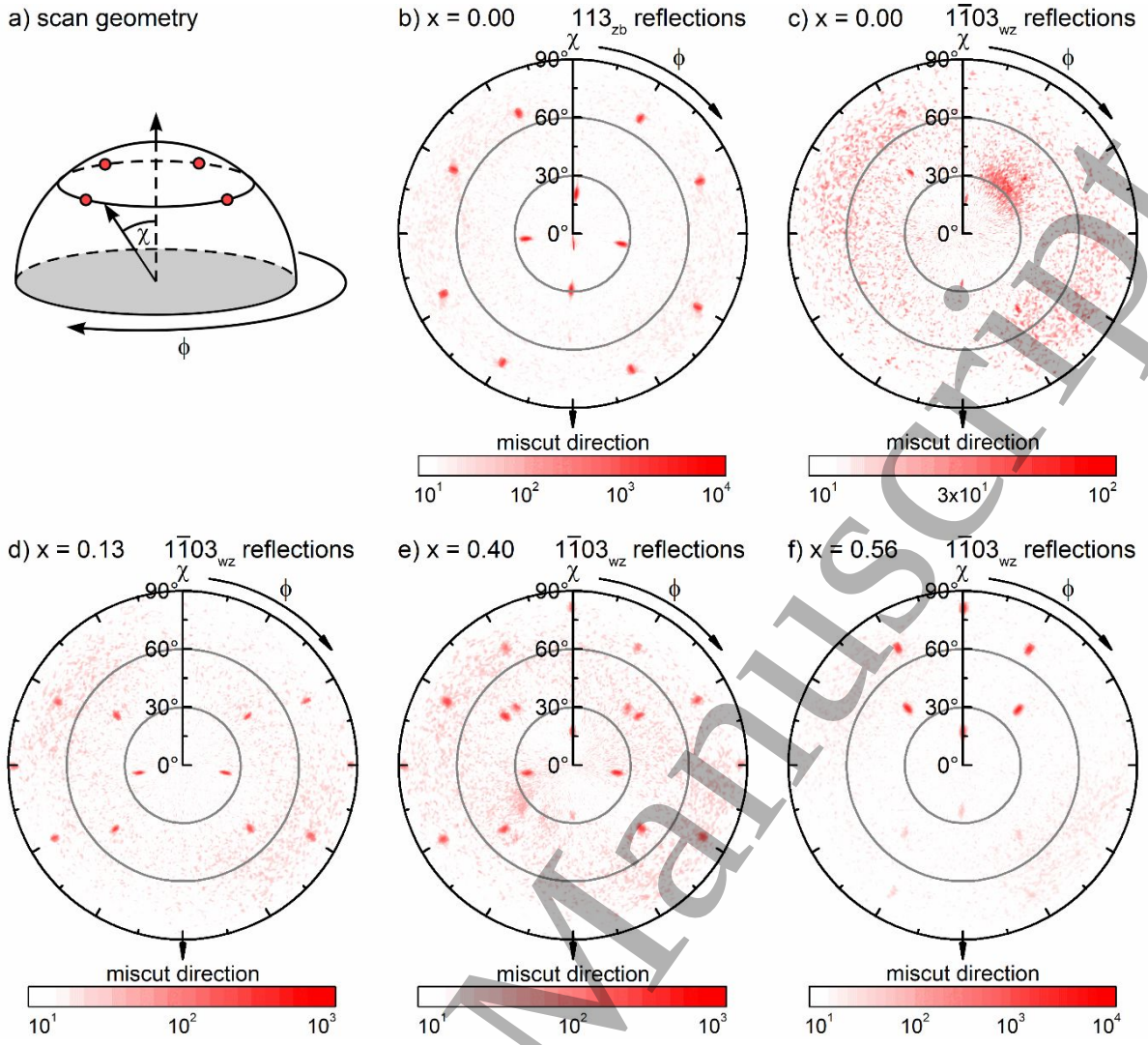

Figure 10: (a) Scan geometry to obtain texture in reciprocal space. Pole figures for 113 zincblende reflections (b) followed by 1$\bar{1}$03 wurtzite reflections of the (001) zb-GaN on $Al_xGa_{1-x}N$ nucleation layers with varying Al fraction of (c) 0, (b) ~0.13, (e) ~0.40 and (f) 0.56.

related to the sample miscut direction. In one of our earlier works, (and as we also have observed in other sample series) we have reported that wurtzite inclusions in zb-GaN on GaN NLs form on the {111} facets inclined perpendicular to the miscut direction [39]. Furthermore, an extensive TEM and XRD study by Lee *et al.* revealed a global anisotropy in the SF distribution with significant more SFs formed on the steepest of the four independent {111} planes in the crystal structure [45]. To examine this behaviour further, we investigate here the influence of the NL alloy composition. For this purpose, we have measured XRD orientational maps of the GaN epilayers grown on $Al_xGa_{1-x}N$ NLs with varying Al fraction between x = 0 and 0.95. This was done by setting the diffractometer to the Bragg angle specific to the cubic zincblende phase or hexagonal wurtzite phase respectively and scanning along the azimuth (φ) and the tilt with respect to the surface (χ) as illustrated in Fig. 10 (a).

Figure 10 (b)-(f) exhibits the measured texture maps for the GaN epilayers grown on various $Al_xGa_{1-x}N$ NLs. The miscut direction was identified from the relative shift of the reflection patterns from both the zb-GaN 113 reflections and the wz 1$\bar{1}$03 reflections in these maps, and is indicated in each case by an arrow pointing downwards. For the GaN buffer grown on the pure GaN NL, the texture map of the 311_{zb} reflections in Fig. 10 (b) shows high intensity zb-GaN reflections forming a pattern highlighting the four-fold symmetry characteristic for the (001) oriented zb-GaN phase. A similar measurement across the $1\bar{1}03_{wz}$ reflections of this sample (Fig. 10 (c)) shows a very weak hexagonal pattern with intensities slightly above the noise level, highlighting the low amount of wurtzite phase. Although the zb phase purity of the film is above 90% (Fig. 9 (b)), a few percent of highly defective zb-GaN material (< 6 vol%) and wurtzite inclusions (< 3 vol%) are present in the film. Any intensity slightly above the noise level leading to the observed pattern have been attributed predominantly to diffuse scattering from SFs, giving a signal at the same position as the $1\bar{1}03_{wz}$ reflections, as discussed in Ref. [29].

A similar trend showing the near absence of clear wz reflections was observed for the two samples grown with $Al_xGa_{1-x}N$ NLs having an Al fraction of x = 0.01 and x = 0.02, respectively (not shown). A schematic representing the cubic

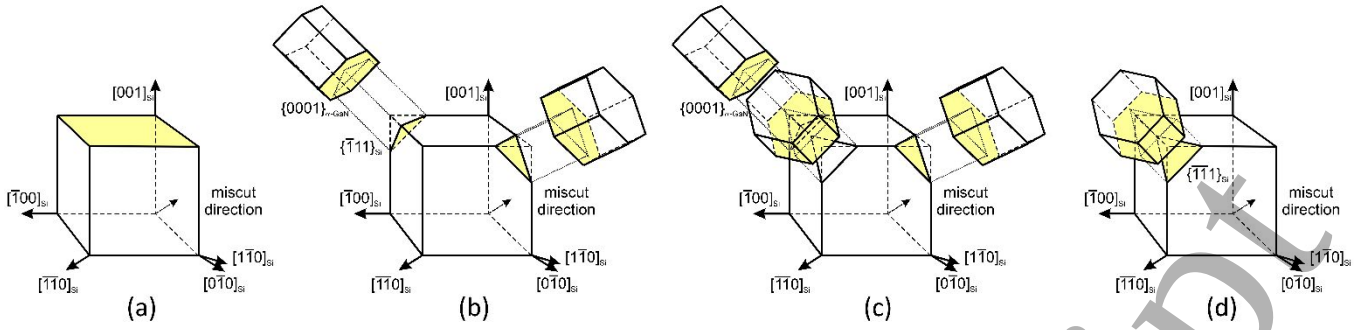

Figure 11: Schematics of (a) zb-GaN [001] growth plane highlighted in yellow, (b) two c-plane wz-GaN basal plane grown on zb-GaN {111}, perpendicular to miscut direction, (c) two c-plane wz-GaN perpendicular and one anti-parallel to miscut direction, and (d) one wz-GaN anti-parallel to miscut direction, corresponding to observed texture maps.

crystal with no wz inclusions is shown in Fig. 11 (a) indicating that the GaN films are in the zb phase (almost) completely at low Al fractions in the NL. In the GaN epilayer with x = 0.13 in the $Al_xGa_{1-x}N$ NL, two distorted wz patterns with six $1\bar{1}03$ wz reflections each were witnessed in the texture map (Fig. 10 (d)) indicating the presence of wz inclusions formed on the two {111} facets which are inclined perpendicular to the miscut direction in the zb-GaN film (Fig. 11 (b)). With further increase of the Al fraction in the NLs to x = 0.40 in Fig. 10 (e), the $1\bar{1}03_{wz}$ reflections of these two types of inclusions in the GaN buffer layer become more intense. Furthermore, a third – slightly weaker – distorted hexagonal pattern of the $1\bar{1}03_{wz}$ reflections can be observed. This pattern is caused by a third type of hexagonal inclusions, which is formed on the shallowest of the four unequal {111} facets, as illustrated in the schematic in Fig. 11 (c). For the GaN epilayer sample with x = 0.56 $Al_xGa_{1-x}N$ NL, the texture map in Fig. 10 (f) reveals highly intense $1\bar{1}03_{wz}$ reflections, attributed to the wz phase, which is formed with its (0001) plane being parallel to the shallowest {111} facet as depicted in Fig. 11 (d). As similar texture maps for the 113 reflections of zb-GaN exhibit no signal attributed to the cubic structure (data not shown), this highlights that the wz phase, in a semipolar orientation, is the only phase present in the GaN layer in this case. The same results have been observed for all other GaN buffer layers grown on $Al_xGa_{1-x}N$ NLs with high Al fraction. The results for low Al fraction NLs are similar to what we have reported before using GaN NLs [30] and confirm that the preferred formation of wurtzite inclusions relates to the sample miscut. In addition, the results from the present study show that wz-phase inclusions form on the {111} facets in different orientations, affected by the alloy composition of the nucleation layer.

Correlating the information on the crystal phase and orientation from the XRD analysis with the morphological information from the AFM analysis enabled us to identify the facet types of the characteristic surface features observed in Fig. 6. For this purpose, we have extracted height profiles from the AFM scans along different crystal directions of the GaN epilayer grown on NLs with high AlN-content. These were compared with the angles between poles in simulated pole figures based on the XRD texture maps (Fig. 10). This analysis revealed that the facets in the GaN epilayer grown on NL with Al fraction of x = 0.40 are (0001) basal planes and $\{1\bar{1}01\}$ planes. By increasing the Al fraction to x = 0.95, a reduction of the basal plane size and increased growth of the $\{1\bar{1}01\}$ planes were observed. Additional TEM analysis is in progress to investigate whether the wz inclusions in the epilayer originate in the nucleation layer or during epilayer growth.

Conclusions

As part of an overall MOVPE growth strategy to reduce the lattice and thermal mismatch between the zb-GaN epilayer and 3C-SiC, the influence of varying Al content of $Al_xGa_{1-x}N$ NL on a 3C-SiC/Si substrate was investigated and its effect on GaN epilayer overgrowth was determined. XPS results of the 15nm thick NLs revealed a significant deviation in the actual NL Al fraction to the nominal values highlighting reduced incorporation of Al due to parasitic pre-reactions. The surface morphology of the NLs transformed from striations along $[1\bar{1}0]$ to granular structures, leading to reduction in surface roughness with increasing Al content. A compressive in-plane strain in the films was measured up to an Al fraction of x = 0.29 at which point the XRD strain analysis of the NLs was limited by the presence of the substrate reflection. No wurtzite reflections were observed in the NL reciprocal space maps up to x = 0.29 showing that the NLs are highly zincblende in phase. However, the low intensity of the $Al_xGa_{1-x}N$ reflections in 2θ-ω measurements for the samples with a higher Al fraction suggested a decline in phase purity. Detailed TEM-based phase analysis investigations of the NLs covering the whole alloy range are currently underway.

The zincblende phase purity of the epilayers remained above 90% for GaN grown on $Al_xGa_{1-x}N$ NL up to an Al content of x = 0.02, after which the phase purity deteriorated due to formation of wurtzite inclusions on various {111} facets of zb-GaN. Further TEM analysis will be required to work out whether this decline in zb phase purity of the epilayer originated within the NL, at the interface between the NL and the overgrown GaN epilayer, or in the epilayer proper.

Acknowledgements

We would like to thank EPSRC for support through grant

no. EP/M010589/1 and grant no. EP/R01146X/1. DJ Wallis would like to acknowledge support through EPSRC fellowship EP/N01202X/2. The authors would also like to thank Mr. Chris Amy for the XPS measurements.

Data availability

The datasets that support the findings of this study are openly available from the University of Cambridge repository at https://doi.org/10.17863/CAM.74541 .

References

1. Lee L Y 2017 Mater. Sci. Tech. 33(14) 1570.
2. Hanada T 2009 Advances in Materials Research 12 Springer Berlin Heidelberg 1.
3. Bougrov V, Levinshtein M E, Rumyantsev S L, and Zubrilov A 2001 John Wiley & Sons, Inc., New York 1.
4. Abe M, Nagasawa H, Potthast S, Fernandez J, Schörmann J, As D J and Lischka K 2006 IEICE Trans. Electron. E89-C, 1057.
5. Vacek P, Frentrup M, Lee L Y, Massabuau F C-P, Kappers M J, Wallis D J, Gröger R, and Oliver R A 2021 J. Appl. Phys. 129 155306.
6. Church S A et al 2017 phys. stat. sol. B 254 1600733.
7. Kemper R M, Veit P, Mietze C, Dempewolf A, Wecker T, Bertram F, Christen J, Lindner J K N, and As D J 2015 Phys. Status Solidi C 12 469.
8. As D J, and Lischka K 2018 Nonpolar Cubic III-nitrides: From the Basics of Growth to Device Applications in Molecular Beam Epitaxy: From Research to Mass Production ed M Henini, (Elsevier).
9. Kimura E, Suzuki T, Ouchi M, Ishida K and Takahashi K 2005 J. Cryst. Growth 278, 411.
10. As D J, Schikora D, and Lischka K 2003 Phys. Status Solidi C 0(6) 1607.
11. Kuznia J N, Yang J W, Chen Q C, Krishnankutty S, Khan M A, George T, and Frietas J Jr 1994 Appl. Phys. Lett. 65(19) 2407994.
12. Wu J, Yaguchi H, KOnabe K, Shiraki, and Ito R 1998 Jpn. J. Appl. Phys. 37, 1440.
13. Yang H, Zheng L X, Li J B, Wang X J, Xu D P, Wang Y T, Hu X W, and Han P D 1999 Appl. Phys. Lett. 74(17) 2498.
14. Strite S, Ruan J, Li Z, Salvador A, Chen H, Smith D J, Choyke W J, and Morkoc H, J. Vac. Sci. Technol. B 9(4) 1924.
15. Trampert A, Brandt O, Yang H, and Ploog K H 1997 Appl. Phys. Lett. 70(5) 583.
16. Okumura H, Ohta K, Feuillet G, Balakrishnan K, Chichibu S, Hamaguchi H, Hacke P and Yoshida S, 1997 J. Cryst. Growth 178 113.
17. D.J. As D J, 2010 Proc. of SPIE 7608 Quantum Sensing and Nanophotonic Devices VII 76080G-15 (2010).
18. Li S, Schormann J, As D J, and Lischka K, 2007 Appl. Phys. Lett. 90 071903
19. As D J, 2009 J. Microelectronics 40 204
20. Martinez-Guerrero E et al 2001 Mat. Sci. Eng. B B82 59.
21. Gerthsen D, Neubauer B, Dieker CH, Lantier R, Rizzi A and Lüth H 1999 J. Cryst. Growth 200 353 (1999).
22. Daudin B et al 1998 J. Appl. Phys. 84 2295.
23. Wu J, Yaguchi H, Nagasawa H, Yamaguchi Y, Onabe K, Shiraki Y and Ito R 1997 Jpn J Appl Phys 36 4241.
24. Gamez-Cuatzin H et al 1999 phys. stat. sol. (a) 176 131.
25. Gerthsen D, Neubauer B, Dieker CH, Lantier R, Rizzi A and Lüth H 1999 J. Cryst. Growth 200 353.
26. Camassel J, Vicente P, Planes N, Allègre J, Pankove J and Namavar F 1999 phys. stat. sol. (b) 216 253.
27. Wei C H, Xie Z Y, Li L Y, Yu Q M and Edgar J H 2000 J. Electron. Mater. 29 317.
28. Kemper R M et al 2011 J. Appl. Phys. 110 123512.
29. Frentrup M, Lee L Y, Sahonta L-S, Kappers M J, Massabuau F, Gupta P, Oliver R A, Humphreys C J and Wallis D J 2017 J. Phys. D Appl. Phys. 50(43) 433002.
30. Lee L Y, Frentrup M, Kappers M J, Oliver R A, Humphreys C J and Wallis D J 2018 J. Appl. Phys. 124(10) 105302.
31. Okumura H, Ohta K, Feuillet G, Feuillet K, Chichibu S, Hamaguchi H, Hacke P and Yoshida S 1997 J. Cryst. Growth 178 113.
32. Zu D, Wallis D J and Humphreys C J 2013 Rep. Pro. Phys 76(10) 106501.
33. Okumura H et al 1998 J. Crystal Growth 189/190 390.
34. Koizumi T, Okumura H, Balakrishnan K, Harima H, Inoue T, Ishida Y, Nagatomo T, Nakashima S and Yoshida S 1999 J. Cryst. Growth 201 341.
35. Gerthsen D, Neubauer B, Dieker CH, Lantier R, Rizzi A and Lüth H, 1999 J. Cryst. Growth 200 353.
36. Städele M, Majewski J A and Vogl P 1997 Phys. Rev. B 56 6911.
37. Schupp T, Rossbach G, Schley P, Goldhahn R, Lischka K and As D J 2010 Phys. Status Solidi C 7 17.
38. As D J 2010 Proc. SPIE 7608 Quantum Sensing and Nanophotonic Devices VII 76080G.
39. Lee L Y, Frentrup M, Vacek P, Massabuau F C-P, Kappers M J, Wallis D J and Oliver R A 2019 J. Cryst. Growth 524 125167.
40. Leitner J, Stejskal J and Sofer Z 2002 phys. stat. sol. (c) 0 (1) 133.
41. Stellmach J, Pristovsek M, Savas O, Schlegel J, Yakovlev E V and Kneissl M 2011 J. Cryst. Growth 315(1) 229.
42. Horcas I, Fernandez R, Gomez-Rodriguez J M, Colchero J, Gomez-Herrero J and Baro A M 2007 Rev. Sci. Instrum. 78 013705.
43. Mishra M, Krishna S, Aggarwal N, Gundimeda A and Gupta G 2017 J. Alloys Compd. 708 385.
44. Iliopoulos E, Ludwig K F, Moustakas T D, Komninou PH, Karakostas TH, Nouet G and Chu S N G, 2001 Mater. Sci. Eng. B 87(3) 227.
45. Lee L Y, Frentrup M, Vacek P, Kappers M J, Wallis D J and Oliver R A 2019 J. Appl. Phys. 125 105303.